

# A next generation upgraded observing platform for the automated Birmingham Solar Oscillations Network (BiSON)

S. J. Hale<sup>a,b</sup>, W. J. Chaplin<sup>a,b</sup>, G. R. Davies<sup>a,b</sup>, and Y. P. Elsworth<sup>a,b</sup>

<sup>a</sup>School of Physics and Astronomy, University of Birmingham, Edgbaston, Birmingham B15 2TT, United Kingdom

<sup>b</sup>Stellar Astrophysics Centre, Department of Physics and Astronomy, Aarhus University, Ny Munkegade 120, DK-8000 Aarhus C, Denmark

## ABSTRACT

The Birmingham Solar Oscillations Network (BiSON) is a collection of ground-based automated telescopes observing oscillations of the Sun. The network has been operating since the early 1990s. We present development work on a prototype next generation observation platform, BiSON:NG, based almost entirely on inexpensive off-the-shelf components, and where the footprint is reduced to a size that can be inexpensively installed on the roof of an existing building. Continuous development is essential in ensuring that automated networks such as BiSON are well placed to observe the next solar cycle and beyond.

**Keywords:** robotic telescope, instrumentation, microelectromechanical systems (MEMS), Internet of Things (IoT), Industry 4.0 protocols, helioseismology, solar oscillations

## 1. INTRODUCTION

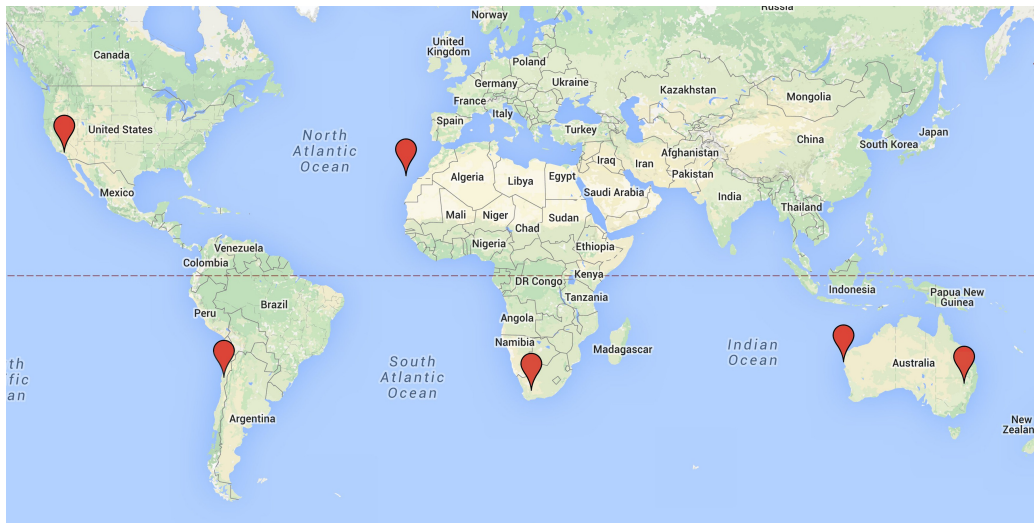


Figure 1. The six station Birmingham Solar Oscillations Network (BiSON). Image credit: Google Maps

The Birmingham Solar Oscillations Network (BiSON) is a collection of ground-based automated solar telescopes observing helioseismic oscillations of the Sun-as-a-star. The network as it stands today was completed in 1992, and consists of six remote sites shown in Fig. 1. A detailed history of the network is available in Ref. 1 and 2. Here, we present development work on a prototype next generation small observation platform,

---

Further author information:

Send correspondence to S. J. Hale <s.j.hale@bham.ac.uk>

BiSON:NG, a significantly miniaturised system based almost entirely on inexpensive consumer-grade off-the-shelf components and commodity hardware.

The existing BiSON solar observatory infrastructure requires a 4 metre observatory dome housing a large equatorial mount. By making use of modern fibre optics it is now possible to split the instrumentation from the front end collection optics, and so allow use of a much smaller mount with considerably lower payload capacity, and subsequently a smaller telescope enclosure. This can be combined with taking advantage of many years of electronic miniaturisation, which has produced micro-controllers and single-board computers allowing old single-purpose hardware to be retired. The resulting physical footprint of BiSON:NG is reduced to a size that can be easily and inexpensively installed on the roof of an existing building, requiring only a small enclosure rather than a dedicated observatory, with no reduction in performance. In the following sections we will discuss some of the key difficulties that have been overcome to allow full automation of consumer-grade astronomy hardware.

## 2. AUTOMATION OF A CONSUMER-GRADE TELESCOPE MOUNT

There are two key issues when attempting to automate a small commercial off-the-shelf (COTS) telescope mount. The first is access to a communications protocol with a published application programming interface (API) in order to allow full computer control of the mount. Many COTS mounts do not have facility for computer control at all, and rely only on the supplied proprietary control handset. In cases where the handset offers an ASCOM compatible control interface this typically does not work without first calibrating the mount position within the handset software, and they offer no facility to store a permanent calibration since they are expected to be packed away at the end of each observing session. Typically movement is tracked by counting stepper-motor steps once initial alignment has been completed, and so the calibration is lost as soon as the mount is moved by hand or the power is interrupted. Larger, more expensive, research-grade mounts employ absolute position encoders to avoid this problem. A fully automated telescope must be able to recover after a power failure without manual recalibration.

The communication and control problem can be solved by simply choosing only manufacturers that open-source and publish their control API. The issue of alignment and recovery from power failure without user intervention is rather more tricky. Potentially a mount could be retro-fitted with absolute position encoders, or limit switches to indicate a home position, but this moves away from the intention of simple off-the-shelf use. Instead, it is possible to make use of microelectromechanical systems (MEMS) sensors to directly detect the attitude of the telescope. Such devices are most commonly used in smartphones and tablets, with accelerometers used to control screen orientation, and magnetometers used to determine heading when navigating. These inexpensive sensors can be easily mounted on the telescope itself and avoid costly modifications to the mount.

A consumer-grade equatorial mount was trialled at the Mount Wilson (Hale) Observatory 60 foot solar tower, an existing BiSON site, in order to determine the possible accuracy of MEMS attitude sensors, and the precision of solar autoguiding.<sup>3</sup> Figure 2, left panel, shows the temporary binocular configuration of fibre collection optics for solar data acquisition, and a solar-filtered CCD camera for guiding. Figure 2, right panel, shows a prototype automated weather-proof housing with a rolling-roof suitable for a small mount and optics. The final design and construction of an enclosure is subject to further work.

In subsection 2.1 below we demonstrate determining telescope attitude from an ADXL345 three-axis accelerometer, in subsection 2.2 acquiring magnetic heading from a HMC5883L three-axis magnetometer, and in subsection 2.3 guiding the mount on the centroid of the solar disc estimated using computer vision techniques.

### 2.1 Determining attitude using a three-axis accelerometer

A MEMS accelerometer measures linear acceleration, and this includes the acceleration due to the Earth's gravitational field vector. Inside the device, a micro proof-mass is suspended by restoring springs, and deflection of the proof-mass due to acceleration is detected by measuring changes in capacitance between the proof-mass and sensing plates. An embedded micro-controller digitises the signal and allows the data to be output over a digital serial bus. A total of three measurement axes are required in order to sense acceleration in all directions. A thorough discussion of calibration of a three-axis accelerometer and extracting pitch and roll angles is given

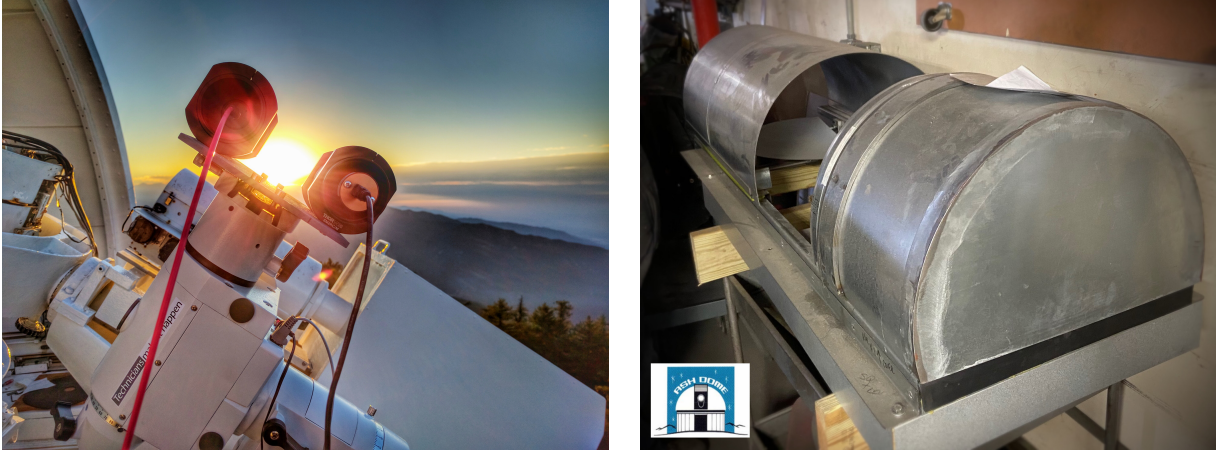


Figure 2. Left: Sunrise at the Mount Wilson (Hale) Observatory.<sup>4</sup> A small consumer-grade equatorial mount was configured with a binocular arrangement of a CCD camera for guiding, and optical fibre collection optics for data acquisition trial. Photo credit: S. J. Hale. Right: A small telescope enclosure and weather-proofing prototype with rolling roof. Photo credit: Ash Manufacturing Company.<sup>5</sup>

in Ref. 6 and 7. We will now summarise the calibration process and go on to apply the techniques to an Analog Devices ADXL345 accelerometer fixed to the optical tube of an equatorially mounted telescope.

The Analog Devices ADXL345 accelerometer is factory calibrated to output values in units of  $g$ , with a precision of 4 milli- $g$  per least-significant bit and a dynamic range of  $\pm 16g$ . The accelerometer measures both the gravitational field vector, and linear acceleration due to motion. Measurement accuracy of the gravitational field is reduced when the device is subject to additional external accelerations, however on a quasi-static design such as a telescope mount this is not a concern. The factory calibration is a 6-term model providing gain and offset parameters for each of the three channels, and this generally provides adequate results in the typical use case of orienting a smartphone. Re-calibrating after the device is installed allows for greater precision to be achieved by correcting for thermal stresses introduced during soldering, and the convenience of allowing installation at an arbitrary angle – the device axes do not need to align with the system axes. A general 12-parameter calibrated output  $\mathbf{G}_{12}$  can be defined in terms of the factory calibration  $\mathbf{G}_f$  by [7, eq. 35],

$$\mathbf{G}_{12} = \begin{pmatrix} G_{12x} \\ G_{12y} \\ G_{12z} \end{pmatrix} = \mathbf{W}\mathbf{G}_f + \mathbf{V} = \begin{pmatrix} W_{xx} & W_{xy} & W_{xz} \\ W_{yx} & W_{yy} & W_{yz} \\ W_{zx} & W_{zy} & W_{zz} \end{pmatrix} \begin{pmatrix} G_{fx} \\ G_{fy} \\ G_{fz} \end{pmatrix} + \begin{pmatrix} V_x \\ V_y \\ V_z \end{pmatrix}, \quad (1)$$

where the gain matrix  $\mathbf{W}$  includes any rotation of the integrated circuit package and also corrects for all possible cross-talk interactions, and  $\mathbf{V}$  are the channel offsets.

If  $M$  measurements are used for the 12-parameter calibration, then the  $i$ -th measurement at pitch angle  $\theta[i]$  and roll angle  $\phi[i]$  becomes [7, eq. 36],

$$\begin{pmatrix} G_{12x}[i] \\ G_{12y}[i] \\ G_{12z}[i] \end{pmatrix} = \begin{pmatrix} W_{xx} & W_{xy} & W_{xz} \\ W_{yx} & W_{yy} & W_{yz} \\ W_{zx} & W_{zy} & W_{zz} \end{pmatrix} \begin{pmatrix} G_{fx}[i] \\ G_{fy}[i] \\ G_{fz}[i] \end{pmatrix} + \begin{pmatrix} V_x \\ V_y \\ V_z \end{pmatrix} = \begin{pmatrix} -\sin(\theta[i]) \\ \cos(\theta[i]) \sin(\phi[i]) \\ \cos(\theta[i]) \cos(\phi[i]) \end{pmatrix}, \quad (2)$$

which can be decomposed into three equations,

$$\begin{aligned} W_{xx}G_{fx}[i] + W_{xy}G_{fy}[i] + W_{xz}G_{fz}[i] + V_x &= -\sin(\theta[i]) \\ W_{yx}G_{fx}[i] + W_{yy}G_{fy}[i] + W_{yz}G_{fz}[i] + V_y &= \cos(\theta[i]) \sin(\phi[i]) \\ W_{zx}G_{fx}[i] + W_{zy}G_{fy}[i] + W_{zz}G_{fz}[i] + V_z &= \cos(\theta[i]) \cos(\phi[i]), \end{aligned} \quad (3)$$

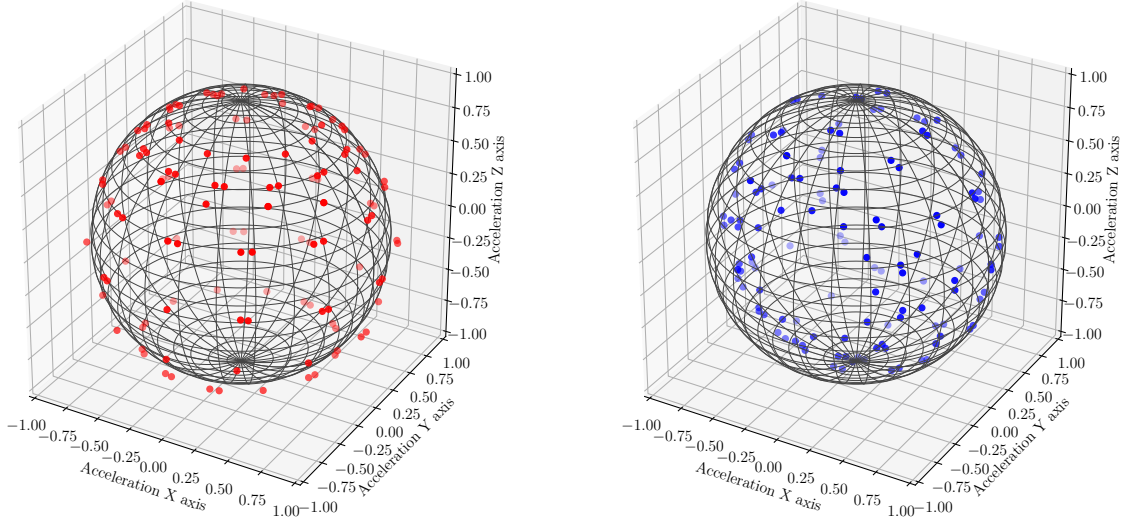


Figure 3. Data from an Analog Devices ADXL345 accelerometer fixed to the optical tube of an equatorially mounted telescope, slewed through its full range of motion. Left: The raw data with standard factory calibration. Right: The data after 12-parameter calibration. All points now sit on the surface of a sphere of radius  $1g$ .

with residuals,

$$\begin{aligned}
 r_x[i] &= -\sin(\theta[i]) - W_{xx}G_{fx}[i] - W_{xy}G_{fy}[i] - W_{xz}G_{fz}[i] - V_x \\
 r_y[i] &= \cos(\theta[i])\sin(\phi[i]) - W_{yx}G_{fx}[i] - W_{yy}G_{fy}[i] - W_{yz}G_{fz}[i] - V_y \\
 r_z[i] &= \cos(\theta[i])\cos(\phi[i]) - W_{zx}G_{fx}[i] - W_{zy}G_{fy}[i] - W_{zz}G_{fz}[i] - V_z .
 \end{aligned} \tag{4}$$

If we now consider only the  $x$ -component, equation 4 can be simplified to [7, eq. 41],

$$r_x = Y_x - \mathbf{X}\beta_x , \tag{5}$$

where  $r_x$  is the  $M$ -length array of residuals to the calibration fit,  $Y_x$  is the array of  $x$ -components of the gravitation field for the true measured angle,  $X$  is the matrix of accelerometer measurements, and finally  $\beta_x$  is the solution vector for four of the calibration parameters. The optimum least squares solution for  $\beta_x$  can be found by making use of the Normal Equations for least squares optimisation,

$$\beta = (\mathbf{X}^T \mathbf{X})^{-1} \mathbf{X}^T \mathbf{Y} , \tag{6}$$

such that [7, eq. 46],

$$\beta_x = \begin{pmatrix} W_{xx} \\ W_{xy} \\ W_{xz} \\ V_x \end{pmatrix} = (\mathbf{X}^T \mathbf{X})^{-1} \mathbf{X}^T Y_x = (\mathbf{X}^T \mathbf{X})^{-1} \mathbf{X}^T \begin{pmatrix} -\sin \theta[0] \\ -\sin \theta[1] \\ \dots \\ -\sin \theta[M-1] \end{pmatrix} , \tag{7}$$

and similarly for the remaining two axes. In order to solve for 12-parameters the minimum number of measurements  $M$  is four, and these should be well distributed in the measurement space. More measurements give a more robust calibration. The calibrated accelerations are subsequently determined using equation 1.

Figure 3 shows a range of measurements made whilst the mount was slewed slowly through its full range of motion. Both factory calibration and improved 12-parameter calibration are shown. The roll and pitch angles can be computed from the calibrated measurement matrix  $\mathbf{G}_{12}$  using [6, eq. 25–26],

$$\phi_{xyz} = \tan^{-1} \left( \frac{G_{12y}}{G_{12z}} \right) , \tag{8}$$

and,

$$\theta_{xyz} = \tan^{-1} \left( \frac{-G_{12x}}{\sqrt{G_{12y}^2 + G_{12z}^2}} \right), \quad (9)$$

where  $\phi$  and  $\theta$  are the measured roll and pitch angles respectively, and the subscript  $xyz$  notes that the angles are according to the aerospace rotation sequence  $\mathbf{R}_{xyz}$  where rotation is first in yaw, then pitch, then roll.

Equation 8 becomes unstable when the telescope is pointing near the zenith, since the  $x$ -axis becomes aligned with the gravitational field vector and enters a condition known as Gimbal Lock. Any rotation in roll can no longer be detected and roll becomes undefined. A common work-around for this problem when using aerospace rotation sequence  $\mathbf{R}_{xyz}$  is to modify equation 8 to include in the denominator a fraction  $\mu$  of the  $x$ -axis measurement whilst remembering to maintain the sign of  $G_{12z}$  after taking the square root [6, eq. 38],

$$\phi_{xyz} = \tan^{-1} \left( \frac{G_{12y}}{\pm \sqrt{G_{12z}^2 + \mu G_{12x}^2}} \right), \quad (10)$$

such that  $\phi$  is slowly driven to zero as the telescope approaches a vertical orientation. An additional ambiguity is caused while the telescope is vertical, since with an equatorial mount it becomes impossible to determine if the telescope is on the east or west side of the pier. This ambiguity can be resolved by the addition of a second accelerometer installed directly on the polar axis of the mount.

In testing, the accelerometer achieved an accuracy of approximately  $\pm 4^\circ$  in pitch and  $\pm 6^\circ$  in roll. The reduced performance in roll is due to the above work-around at high pitch angles. Performance from both axes is similar if only moderate pitch angles are considered. Mészáros et. al. trialled the two-accelerometer technique by mounting two Freescale MMA8453Q accelerometers on their telescope at Konkoly Observatory located at the Piszkestető Mountain station,<sup>8</sup> and achieved accuracy to better than a degree with more sophisticated calibration, by making use of full temperature compensation, and taking good care of power supply stability via a custom printed circuit board. The simpler treatment shown here is adequate for a solar autoguider with a capture angle of a few degrees.

Accelerometers are capable of completely resolving telescope attitude only with an equatorial telescope mount. With an altitude-azimuth mount, only changes in altitude (pitch) can be measured. Rotations in azimuth (yaw) are aligned with the gravitational field vector and cannot be detected, and so a different sensor is required. Next, we look at using a three-axis magnetometer to detect the orientation of Earth’s magnetic field and directly measure the telescope “heading” angle.

## 2.2 Determining heading using a three-axis magnetometer

In order to detect rotation about a vector parallel to Earth’s gravitational field vector (i.e., yaw, heading, azimuth) we need to be able to detect rotation within Earth’s magnetic field, otherwise known as an electronic compass. We used a Honeywell HMC5883L three-axis magnetometer, which uses magneto-resistive sensors to measure both the direction and the magnitude of Earth’s magnetic field. The Honeywell HMC5883L magnetometer is factory calibrated to output values in units of  $\mu\text{T}$ , with a dynamic range of  $800 \mu\text{T}$ , and an embedded 12-bit ADC providing a documented  $1^\circ$  to  $2^\circ$  heading accuracy. As with the accelerometer, a magnetometer requires a final in-situ calibration in order to achieve the best precision. A thorough discussion of calibration of a three-axis magnetometer is given in Refs. 9–12. We will now summarise the calibration process and go on to apply the techniques to the Honeywell HMC5883L, including tilt-compensation based on earlier results from the Analog Devices ADXL345 accelerometer.

A magnetic vector measured at the device  $\mathbf{B}_d$  can be defined after arbitrary device rotation in terms of the local geomagnetic field vector  $\mathbf{B}$  by [9, eq. 5],

$$\mathbf{B}_d = \mathbf{W} \mathbf{R}_x(\phi) \mathbf{R}_y(\theta) \mathbf{R}_z(\psi) \|\mathbf{B}\| \begin{pmatrix} \cos \delta \\ 0 \\ \sin \delta \end{pmatrix} + \mathbf{V}, \quad (11)$$

where  $\phi$ ,  $\theta$ , and  $\psi$  are roll, pitch, and yaw angles as previously,  $\delta$  is the magnetic inclination at the measurement location,  $\mathbf{V}$  is the “hard-iron” offset vector, and  $\mathbf{W}$  is the “soft-iron” gain matrix. So-called hard-iron offsets are



magnetic fields generated by nearby permanent magnets, such as other components on the PCB, and motors in the telescope mount. These components are generally in fixed positions and rotate with the device, and so they appear as an additive magnetic field vector within the reference frame of the magnetometer. So-called soft-iron interference is due to temporary induction of magnetic fields in otherwise normally unmagnetised components, such as the sheet steel of the telescope mount and housing, caused by the geomagnetic field itself. Soft-iron effects are much more complicated to model since they depend on the orientation of the device within the geomagnetic field, and typically suffer magnetic hysteresis effects as the device rotates. The soft-iron matrix  $\mathbf{W}$  is a 9-element matrix similar to that used during calibration of the accelerometer in equation 1, and in addition to calibrating soft-iron effects also calibrates rotation of the integrated circuit package and corrects for all possible cross-talk interactions and gain variations between channels. In addition to removing offsets, the measurements from a magnetometer need to be derotated back to the flat plane where  $\phi = \theta = 0$ , since as with a typical analogue compass it works only when held level. Rearranging equation 11 for  $\psi$  we get [9, eq. 6],

$$\begin{aligned} \mathbf{R}_z(\psi)\|\mathbf{B}\| \begin{pmatrix} \cos \delta \\ 0 \\ \sin \delta \end{pmatrix} &= \begin{pmatrix} \cos \psi & \sin \psi & 0 \\ -\sin \psi & \cos(\psi) & 0 \\ 0 & 0 & 1 \end{pmatrix} \|\mathbf{B}\| \begin{pmatrix} \cos \delta \\ 0 \\ \sin \delta \end{pmatrix} \\ &= \mathbf{R}_y(-\theta)\mathbf{R}_x(-\phi)\mathbf{W}^{-1}(\mathbf{B}_d - \mathbf{V}) , \end{aligned} \quad (12)$$

and so [9, eq. 9],

$$\begin{pmatrix} B_{fx} \\ B_{fy} \\ B_{fz} \end{pmatrix} = \begin{pmatrix} \cos \psi \cos \delta \|\mathbf{B}\| \\ -\sin \psi \cos \delta \|\mathbf{B}\| \\ \sin \delta \|\mathbf{B}\| \end{pmatrix} = \mathbf{R}_y(-\theta)\mathbf{R}_x(-\phi)\mathbf{W}^{-1}(\mathbf{B}_d - \mathbf{V}) , \quad (13)$$

where  $\mathbf{B}_f$  is equal to the magnetometer measurements with both soft-iron and hard-iron effects removed, and derotated to a flat plane where the  $z$ -component  $B_{fz}$  is equal to  $\|\mathbf{B}\| \sin \delta$ . The yaw angle, or compass heading, is found from [9, eq. 10],

$$\psi = \tan^{-1} \left( \frac{-B_{fy}}{B_{fx}} \right) , \quad (14)$$

and this simply requires the addition of the known local magnetic declination to convert from magnetic north to true north, and so obtain the azimuthal angle.

In many cases the soft-iron effects are insignificant, and only the hard-iron offsets dominate. This allows a simplification during calibration since only four parameters need to be determined, and these are the magnitude of the geomagnetic field strength  $\|\mathbf{B}\|$ , and the three components of the hard-iron vector  $\mathbf{V}$ . The soft-iron matrix  $\mathbf{W}$  becomes the identity matrix. With these assumptions we can follow the same calibration procedure as for the accelerometer, by developing a performance function to be minimised by optimising the calibration fit and again using equation 6 to solve the fit through matrix algebra.

Figure 4 shows a range of measurements made by a Honeywell HMC5883L magnetometer slewed randomly through the full range of motion. It is clear from the left panel of Figure 4 that the data do indeed suffer from a hard-iron offset, which moves the data away from the origin. After applying the 4-parameter calibration, shown by the blue dots in the right panel of Figure 4, the data now sit on the surface of a sphere centred at the origin, with radius equal to the local geomagnetic field strength in Birmingham calibrated at 54.5  $\mu\text{T}$ . Our assumption that the soft-iron effects are insignificant is shown to be true, since these would have the effect of distorting the data away from a perfect sphere and into an ellipse. The green dots show the same data after derotation, by making use of the pitch and roll angles determined by the accelerometer, to the flat plane where  $\phi = \theta = 0$  and the  $z$ -component  $B_{fz}$  is equal to  $\|\mathbf{B}\| \sin \delta$ . These data are now calibrated and ready for the heading to be extracted using equation 14. The resulting accuracy after calibration is approximately  $\pm 5^\circ$ . With further work and more careful calibration, it is expected to achieve the manufacturers stated performance of  $1^\circ$  to  $2^\circ$  resolution. With this simple calibration, and as with the accelerometer, the performance is adequate for a solar autoguiding with a capture angle of a few degrees.

Having shown that it is possible to obtain sufficiently accurate absolute pointing information of an inexpensive telescope mount at power-on, we will now go on to consider fine guiding of a mount once the target has been acquired by the coarse pointing.

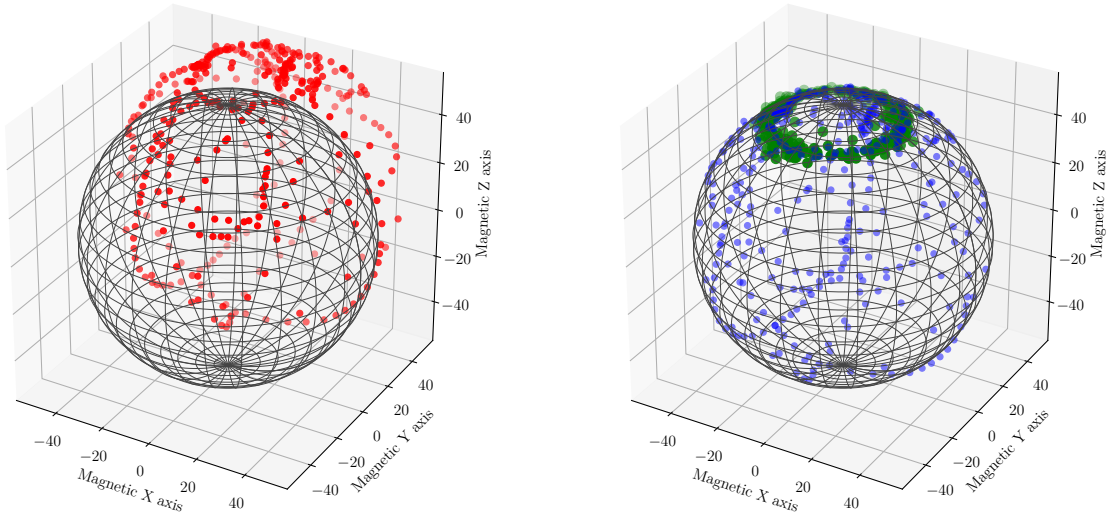


Figure 4. Data from a Honeywell HMC5883L magnetometer slewed randomly through the full range of motion. Left: The raw data with a hard-iron offset. Right: The blue dots show the data after 4-parameter calibration removing the hard-iron offset. All points now sit on the surface of a sphere centred at the origin, with radius equal to the local geomagnetic field strength in Birmingham calibrated at  $54.5 \mu\text{T}$ . The green dots show the same data after derotation to the flat plane where  $\phi = \theta = 0$  and the  $z$ -component  $B_{fz}$  is equal to  $\|\mathbf{B}\| \sin \delta$ .

### 2.3 Solar auto-guiding using computer vision

After the Sun is brought within the capture angle of the autoguiding camera by the coarse MEMS-based pointing, mount control is handled purely via imaged-based guiding much like any other telescope. The camera trialled has a  $6.4 \text{ mm}$  by  $4.75 \text{ mm}$  CCD with  $4.65 \mu\text{m}$  square pixels in a  $1392$  by  $1040$  array. When coupled with an  $80 \text{ mm}$  focal length objective lens this produces an approximate field of view of  $4.6^\circ$  by  $3.5^\circ$ , where each pixel has about  $12''$  field of view. The Sun has an extent of about  $32'$  and so produces an image about  $160$  pixels in diameter on the sensor. Two filters were used to bring the image within the dynamic range of the CCD chip. These were a neutral density filter with optical density of  $5$  (i.e, transmission of approximately  $10^{-5}$ ), and a  $10 \text{ nm}$  bandpass filter centered on  $780 \text{ nm}$ . Images were read from the camera as frequently as possible, approximately once per second. The image exposure time was  $79 \text{ ms}$ , but the cadence was restricted by the CCD read-out time and USB transfer rate.

Images from the camera were processed to determine the position of the Sun to sub-pixel accuracy using the OpenCV (Open-source Computer-Vision) library,<sup>13</sup> running on an inexpensive single-board-computer. The centroid position of the solar disc was found using by applying a black and white threshold, finding the contours in the image, and subsequently reading out the contour centroid position. The guiding error was determined by comparing the current solar centroid position with a desired target value. The position error for each axis was then passed through a proportional-integral-derivative (PID) control loop feedback mechanism in order to determine the correct mount drive rate, and the mount motors updated with the new drive rate using the motor API published by the mount manufacturer. The PID control algorithm is a servo feedback system that can be defined simply by,

$$\text{Output} = K_P e(t) + K_I \int e(t) dt + K_D \frac{de(t)}{dt}, \quad (15)$$

where  $e$  is the control error defined as the desired setpoint minus the current value, and  $K_P$ ,  $K_I$ , and  $K_D$  are the proportional, integral, and derivative coefficients. The solar guiding algorithm made use of only the proportional and integral parameters.

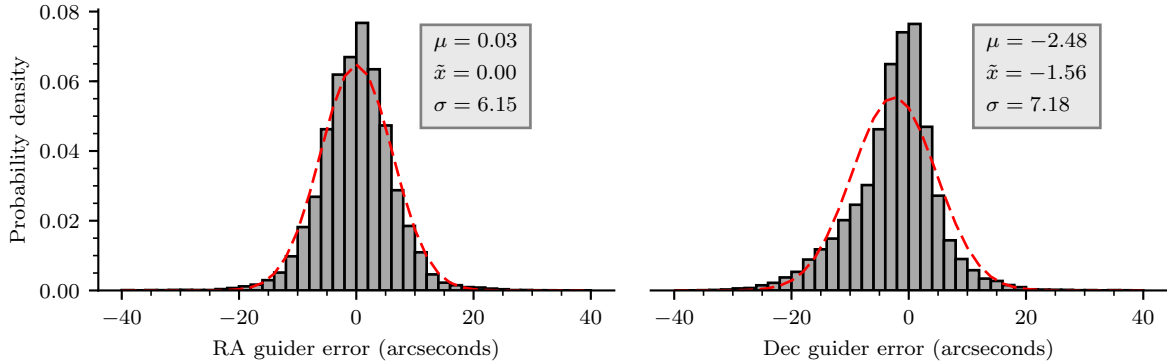


Figure 5. Guider performance histogram. The dashed red line indicates the equivalent Gaussian for the measured median and standard deviation.

The distribution of position-error for both axes, calibrated in arcseconds, is shown in Figure 5. The control algorithm achieves performance on both axes to better than  $\pm 8''$  when logged at an approximate 1 Hz cadence over an entire day. This is more than sufficient for Sun-as-a-star observations when considering the Sun is over  $1800''$  in observed diameter.

By making use of these techniques it is possible to achieve full automation of consumer-grade telescope mounts. In the next section we will discuss prototype updates to the BiSON control systems.

### 3. SUPERVISORY CONTROL AND DATA ACQUISITION

In the early 1990s, the original network control system was based around a standard desktop PC running Microsoft DOS, and a Keithley System 570 digital input/output interface for connection to dome, telescope, and instrumentation control hardware. The computer acted as a centralised controller, handling all systems from dome and mount pointing, to temperature stabilisation and data readout, using a Supervisory Control and Data Acquisition (SCADA) monolithic control system architecture. The data would be retrieved each day over a long-distance telephone call via dial-up modem, and later over the internet. The Keithley interface devices were used until 2002, when the DOS PCs were replaced with the current systems running GNU/Linux with hardware interconnects predominately via RS-232, although a PCI general purpose digital-IO card is still used to interface to some legacy equipment.

The so-called “Industry 4.0”, the fourth industrial revolution, has since brought about inter-connected machines, devices, and sensors – the “Internet of Things” (IoT) – that have allowed control systems to become decentralised. By migrating from a monolithic to a microservice based architecture (MSA) in a Distributed Control System (DCS) it is possible to further reduce both the physical footprint, complexity, and deployment cost. A microservice follows the Unix philosophy of “Do One Thing and Do It Well”, where each service is a single purpose process capable of handling a request independently. Such decoupled processes allow a modular approach to system design, reducing development into more manageable components and removes the need to understand the entire monolithic system. Independent modules also mean they can be independently upgraded or replaced, removing the common risk of being forced to redesign an entire system simply because one component has become obsolete. When all devices and sensors are connected to every other service, it can also become possible trigger maintenance processes autonomously by monitoring data from all points in the overall system and predicting potential failures. Such flexibility is essential in the operation of a worldwide constellation of small telescopes, that inevitably become heterogeneous due to gradual roll-out of repairs and upgrades. Figure 6 shows a block diagram of the proposed MSA for BiSON:NG, and also for implementation at the existing network telescopes.

Communication between microservices is typically handled using lightweight protocols with well-defined inputs and outputs. Most IoT devices communicate over internet protocol networks making use of industry



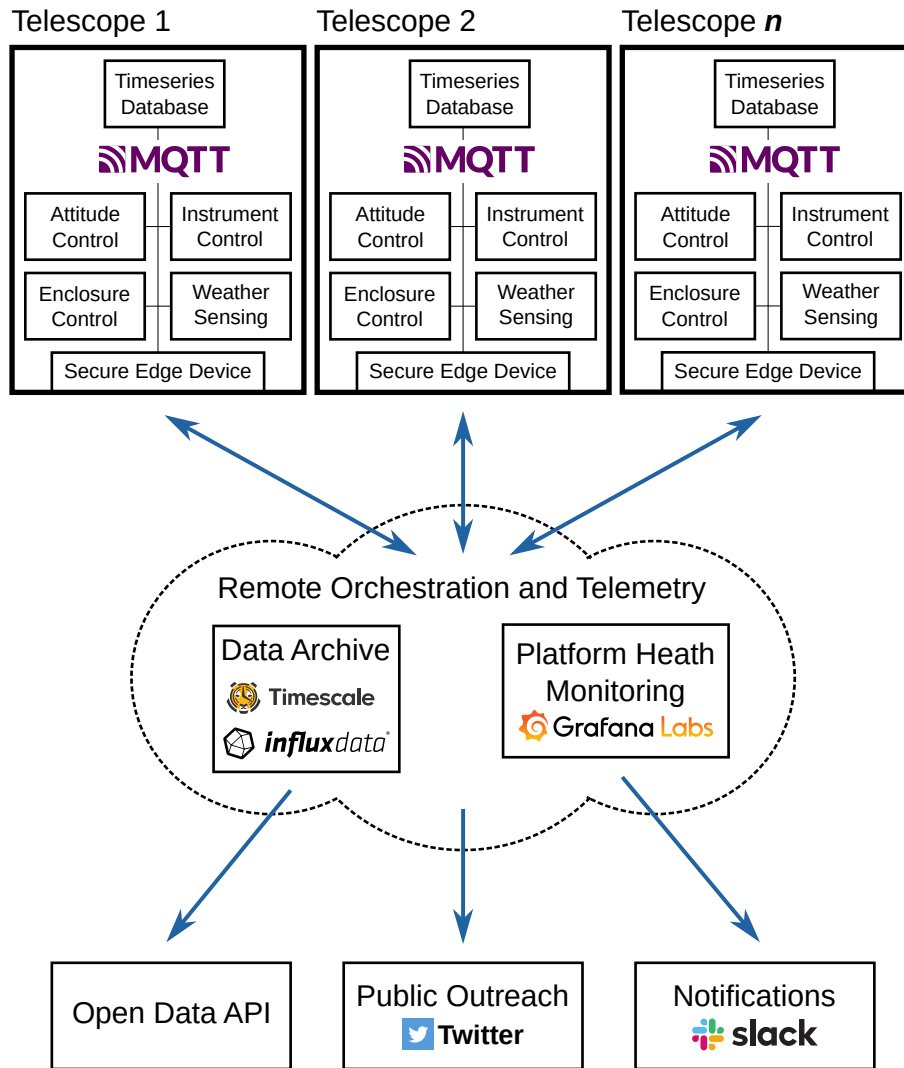


Figure 6. A block diagram of the proposed microservice architecture for BiSON:NG, that is easily scalable to many small telescopes in a globally distributed network.

standard Ethernet or WiFi. This has a significant advantage in allowing many devices to be easily connected using standard network switches, rather than relying on the limited connectivity options available on a single PC. Components such as sensors and controllers from different manufacturers need to communicate using standardised communication protocols. As is common with standards there are several from which to choose, such as OPC UA (Open Platform Communications Unified Architecture), DDS (Data Distribution Service), MQTT (Message Queuing Telemetry Transport), CoAP (Constrained Application Protocol), Extensible Messaging and Presence Protocol (XMPP), Advanced Message Queuing Protocol (AMQP), and others.<sup>14</sup> Whilst there is no one best protocol, we have chosen to use MQTT due to it being designed for low-bandwidth connections from remote locations. It is extremely lightweight, with open source examples of implementation on micro-controllers where a small code footprint is essential, and single-board computers, both of which we use extensively.

MQTT is an ISO standard client/server publish/subscribe protocol developed by IBM.<sup>15</sup> The protocol requires a message broker through which clients communicate, with messages organised into topics. Messages are broadcast on a one-to-many distribution basis. The protocol can scale easily up to hundreds or even thousands of devices, allowing decoupling of applications since any service with an interest in a particular data feed can simply subscribe to the relevant topic. Several quality-of-service (QoS) options are available, ensuring messages

are delivered either at most once, at least once, or exactly once, providing robust communication even over high-latency or unreliable networks. Typically only a single broker is required, although multiple brokers can be linked for either redundancy, load sharing, or connecting between local and remote sites. There are also security advantages to using MQTT, since communication can be easily authenticated over a Transport Layer Security (TLS) encrypted channel. The broker manages all security credentials and certificates, and also tracks the client connection states allowing rapid notification of a disconnected service.

A number of free and open-source packages are used where possible. Data archival is handled both locally at each telescope, in order to survive network outages, and remotely for aggregation. A timeseries-specific database is used, such as Timescale<sup>16</sup> and InfluxDB,<sup>17</sup> to ensure performance at scale. Platform monitoring and telemetry visualisation is produced by Grafana,<sup>18</sup> with system log messages written locally and, where necessary, published to a Slack<sup>19</sup> channel for urgent notification. Public outreach is possible through automatic status updates via social media such as Twitter.<sup>20</sup>

Through the upgrades discussed here, we move from a full rack of electronics to physically small services closely coupled near their respective areas of instrumentation.

## 4. CONCLUSION

The Birmingham Solar Oscillations Network has achieved an average annual duty cycle of around 82% since commissioning in 1992, providing an unparalleled baseline of unresolved-Sun helioseismic observations.<sup>1</sup> The aim of observing potential solar gravity-modes ( $g$ -modes) requires much lower noise levels over long time periods than currently achieved by any Sun-as-a-star observations, since they are expected to have very low amplitudes and low frequencies.<sup>21</sup> The instrumental noise level is dominated by atmospheric scintillation<sup>22</sup> and that of solar origin, but both can be beaten down by combining multiple incoherent measurements from many simultaneous observations,<sup>23,24</sup> and so there is a need to considerably increase the number of BiSON observing sites.

We have shown here that it is possible to achieve full automation of an inexpensive consumer-grade telescope mount through the addition of MEMS inertial sensors, within a small physical package requiring only a basic weather-proof automated enclosure. A microservices control architecture allows the control systems to run entirely on inexpensive single-board computers and micro-controllers, removing the need for a full rack of electronics and again reducing cost. Initial trials of these small form factor techniques at three existing BiSON sites have shown an improvement in performance through the reduction of certain noise sources such as guider errors.<sup>2,25-28</sup> In order to ensure that BiSON is well placed to observe the next solar cycle and beyond, continuous development and improvement is essential.

The impact of BiSON:NG extends far wider than the field of solar astronomy. A large network of small inexpensive robotic telescopes can easily be made dual purpose, for both solar and stellar astronomy. Telescopes as small as 6 inches have research applications where, perhaps operated by schools and Citizen Scientists, they are capable of follow-up observations of exoplanet transits.<sup>29,30</sup> Dramatically increasing the number of telescopes available to students for education, outreach, and public engagement makes it possible for young people to access and participate in research, and can help to encourage people from all backgrounds into a science career.<sup>31-33</sup> BiSON:NG offers an unprecedented opportunity for multifaceted science, engagement, and collaboration.

## ACKNOWLEDGMENTS

We would like to thank all those who have been associated with BiSON over the years. We particularly acknowledge the technical assistance at our remote network sites, with sincere apologies to anyone inadvertently missed: At Mount Wilson: Ed J. Rhodes, Jr., Stephen Pinkerton, the team of USC undergraduate observing assistants, former USC staff members Maynard Clark, Perry Rose, Natasha Johnson, Steve Padilla, and Shawn Irish, and former UCLA staff members Larry Webster and John Boyden. At Las Campanas: Patricio Pinto, Andres Fuentesvilla, Emilio Cerda, Frank Perez, Marc Hellebaut, Patricio Jones, Gastón Gutierrez, Juan Navarro, Francesco Di Mille, Roberto Bermudez, and the staff of LCO. At Izaña: Pere Pallé, Teo Roca Cortés, Antonio Pimienta, and the team of operators who have contributed to running the Mark I instrument over many years. At Sutherland: Pieter Fourie, Willie Koorts, Jaci Cloete, Reginald Klein, John Stoffels, Brendt Christian, and the staff of SAAO. At Carnarvon: Les Bateman, Les Schultz, Sabrina Dowling-Giudici, Inge Lauw of Williams and

Hughes Lawyers, and NBN Co. Ltd. At Narrabri: Mike Hill and the staff of CSIRO. The authors are grateful for the financial support of the Science and Technology Facilities Council (STFC), grant reference ST/R000417/1. Additional funding was secured via the STFC Impact Accelerator account, with the assistance of Alan Tibbatts from University of Birmingham Enterprise. Funding for the Stellar Astrophysics Centre (SAC) is provided by The Danish National Research Foundation, grant reference DNRF106.

## REFERENCES

- [1] Hale, S. J., Howe, R., Chaplin, W. J., Davies, G. R., and Elsworth, Y. P., “Performance of the Birmingham Solar-Oscillations Network (BiSON),” *Sol. Phys.* **291**, 1–28 (Jan. 2016).
- [2] Hale, S. J., *Birmingham Solar Oscillations Network: The Next Generation*, PhD thesis, School of Physics and Astronomy, University of Birmingham, UK (July 2019).
- [3] Hale, S. J., “Fibre-feed tests at Mount Wilson in 2016 September,” BiSON Technical Report Series, Number 382, High-Resolution Optical-Spectroscopy Group, University of Birmingham, UK (Dec. 2016).
- [4] Hale, S. J., “Sunrise on Research.” Gatsby Charitable Foundation Trust (May 2017).
- [5] Ash Manufacturing Company, “Observatories and tracking instrument shelters,” (Sept. 2020).
- [6] Pedley, M., “Tilt Sensing Using a Three-Axis Accelerometer,” Application Note 3461, Freescale Semiconductor, Inc. (Mar. 2013).
- [7] Pedley, M., “High-Precision Calibration of a Three-Axis Accelerometer,” Application Note 4399, Freescale Semiconductor, Inc. (Oct. 2015).
- [8] Mészáros, L., Jaskó, A., Pál, A., and Csépany, G., “Accurate Telescope Mount Positioning with MEMS Accelerometers,” *PASP* **126**, 769–782 (Aug. 2014).
- [9] Ozyagcilar, T., “Calibrating an eCompass in the Presence of Hard- and Soft-Iron Interference,” Application Note 4246, Freescale Semiconductor, Inc. (Nov. 2015).
- [10] Ozyagcilar, T., “Layout Recommendations for PCBs Using a Magnetometer Sensor,” Application Note 4247, Freescale Semiconductor, Inc. (Nov. 2015).
- [11] Ozyagcilar, T., “Implementing a Tilt-Compensated eCompass using Accelerometer and Magnetometer Sensors,” Application Note 4248, Freescale Semiconductor, Inc. (Nov. 2015).
- [12] Ozyagcilar, T., “Accuracy of Angle Estimation in eCompass and 3D Pointer Applications,” Application Note 4249, Freescale Semiconductor, Inc. (Nov. 2015).
- [13] Bradski, G., “The OpenCV Library,” *Dr. Dobb’s Journal of Software Tools* (2000).
- [14] Profanter, S., Tekat, A., Dorofeev, K., Rickert, M., and Knoll, A., “OPC UA versus ROS, DDS, and MQTT: Performance Evaluation of Industry 4.0 Protocols,” in *[2019 IEEE International Conference on Industrial Technology (ICIT)]*, 955–962 (2019).
- [15] International Organization for Standardization, “Information technology — Message Queuing Telemetry Transport (MQTT) v3.1.1,” (June 2016).
- [16] Timescale, “PostgreSQL for time-series,” (Oct. 2018).
- [17] InfluxData, “InfluxDB: An open-source time series database,” (Sept. 2013).
- [18] Grafana Labs, “Grafana: The open observability platform,” (2014).
- [19] Slack Technologies, “Slack: Brings all your communication together,” (Aug. 2013).
- [20] Twitter, Inc., “Twitter: A microblogging and social networking service,” (Mar. 2006).
- [21] Appourchaux, T., Belkacem, K., Broomhall, A. M., Chaplin, W. J., Gough, D. O., Houdek, G., Provost, J., Baudin, F., Boumier, P., Elsworth, Y., García, R. A., Andersen, B. N., Finsterle, W., Fröhlich, C., Gabriel, A., Grec, G., Jiménez, A., Kosovichev, A., Sekii, T., Toutain, T., and Turck-Chièze, S., “The quest for the solar g modes,” *A&A Rev.* **18**, 197–277 (Feb. 2010).
- [22] Hale, S. J., Chaplin, W. J., Davies, G. R., Elsworth, Y. P., Howe, R., and Pallé, P. L., “Measurement of Atmospheric Scintillation during a Period of Saharan Dust (Calima) at Observatorio del Teide, Izaña, Tenerife, and the Impact on Photometric Exposure Times,” *PASP* **132**, 034501 (Jan. 2020).
- [23] Davies, G. R., Chaplin, W. J., Elsworth, Y., and Hale, S. J., “BiSON data preparation: a correction for differential extinction and the weighted averaging of contemporaneous data,” *MNRAS* **441**, 3009–3017 (July 2014).

- [24] Lund, M. N., Chaplin, W. J., Hale, S. J., Davies, G. R., Elsworth, Y. P., and Howe, R., “Spatial incoherence of solar granulation: a global analysis using BiSON 2B data,” *MNRAS* **472**, 3256–3263 (Dec. 2017).
- [25] Hale, S. J., “Fibre-feed tests at Izaña in 2017 May,” BiSON Technical Report Series, Number 384, High-Resolution Optical-Spectroscopy Group, University of Birmingham, UK (Sept. 2017).
- [26] Hale, S. J., “Fibre-feed tests at Izaña in 2017 September,” BiSON Technical Report Series, Number 385, High-Resolution Optical-Spectroscopy Group, University of Birmingham, UK (Sept. 2017).
- [27] Hale, S. J. and Ross, E., “Jabba fibre conversion at Carnarvon in 2018 April,” BiSON Technical Report Series, Number 389, High-Resolution Optical-Spectroscopy Group, University of Birmingham, UK (June 2018).
- [28] Hale, S. J., “Klaus fibre conversion at Mount Wilson in 2018 June,” BiSON Technical Report Series, Number 390, High-Resolution Optical-Spectroscopy Group, University of Birmingham, UK (Aug. 2018).
- [29] Dragomir, D., Harris, M., Pepper, J., Barclay, T., Villanueva, S., Ricker, G. R., Vanderspek, R., Latham, D. W., Seager, S., Winn, J. N., Jenkins, J. M., Ciardi, D. R., Furesz, G., Henze, C. E., Mireles, I., Morgan, E. H., Quintana, E. V., Ting, E. B., and Yahalomi, D., “Securing the Legacy of TESS through the Care and Maintenance of TESS Planet Ephemerides,” *The Astronomical Journal* **159**, 219 (Apr. 2020).
- [30] Zellem, R. T., Pearson, K. A., Blaser, E., Fowler, M., Ciardi, D. R., Biferno, A., Massey, B., Marchis, F., Baer, R., Ball, C., Chasin, M., Conley, M., Dixon, S., Fletcher, E., Hernandez, S., Nair, S., Perian, Q., Sienkiewicz, F., Tock, K., Vijayakumar, V., Swain, M. R., Roudier, G. M., Bryden, G., Conti, D. M., Hill, D. H., Hergenrother, C. W., Dussault, M., Kane, S. R., Fitzgerald, M., Boyce, P., Peticolas, L., Gee, W., Cominsky, L., Zimmerman-Brachman, R., Smith, D., Creech-Eakman, M. J., Engelke, J., Iturralde, A. r., Dragomir, D., Jovanovic, N., Lawton, B., Arbouch, E., Kuchner, M., and Malvache, A., “Utilizing Small Telescopes Operated by Citizen Scientists for Transiting Exoplanet Follow-up,” *PASP* **132**, 054401 (May 2020).
- [31] Sadler, P. M., Gould, R. R., Leiker, P. S., Antonucci, P. R. A., Kimberk, R., Deutsch, F. S., Hoffman, B., Dussault, M., Contos, A., Brecher, K., and French, L., “MicroObservatory Net: A Network of Automated Remote Telescopes Dedicated to Educational Use,” *Journal of Science Education and Technology* **10**, 39–55 (Mar 2001).
- [32] Gould, R. R., Sunbury, S., Sienkiewicz, F., Deutsch, F., Ibrahim, A., Dussault, M., and Krumhansl, R., “The Other Worlds Project: Students Detect Exoplanets Using the MicroObservatory Online Telescopes,” in [*Earth and Space Science: Making Connections in Education and Public Outreach*], Jensen, J. B., Manning, J. G., and Gibbs, M. G., eds., *Astronomical Society of the Pacific Conference Series* **443**, 162 (Sept. 2011).
- [33] Gomez, E. L. and Fitzgerald, M. T., “Robotic telescopes in education,” *The Astronomical Review* **13**, 28–68 (Jan. 2017).